Misorientation Control and Functionality Design of Nanopillars in Self-Assembled Perovskite–Spinel Heteroepitaxial Nanostructures

Sheng-Chieh Liao,[†] Pei-Yu Tsai,[‡] Chen-Wei Liang,[‡] Heng-Jui Liu,[†] Jan-Chi Yang,[‡] Su-Jien Lin,[†] Chih-Huang Lai,[†] and Ying-Hao Chu[‡,*]

[†]Department of Materials Science and Engineering, National Tsing Hua University, Hsinchu 30013, Taiwan, and [‡]Department of Materials Science and Engineering, National Chiao Tung University, Hsinchu 30010, Taiwan

I n complex, correlated oxides, the coupling between lattice, charge, orbital, and spin degrees of freedom shows novel physical phenomena.[1] Heterointerfaces provide a powerful route to manipulate these degrees of freedom.[2] In artificially fabricated heterointerfaces, including layered structures and vertical nanostructures, interaction of these degrees of freedom results in a number of exciting discoveries, *e.g.*, two-dimensional electron gas at the oxide interface,[3] ferromagnetic order at the superconductor–ferromagnet superlattice,[4] and strong magnetoelectric coupling in multiferroic nanostructure.[5] The lattice misorientation of the constituent materials of these heterostructures plays a decisive role in determining the electronic and/or magnetic couplings at the oxide interfaces. However, we notice that new physics observed in oxide heterostructures thus far have been studied only of the constituent materials with the same crystallographic orientations in each system, which is solely determined by the substrate.[6–8] An interesting question arises: Can we control the relative lattice orientation of the constituent oxides in order to create interfaces with various crystallographic relationships in the heterostructures? This is also an important question because a structurally tunable oxide interface expands the degrees of freedom in terms of lattice coupling and allows experimental studies of fundamental physics emerging therefrom. To answer this question, we chose a columnar $CoFe_2O_4$–$BiFeO_3$ heterostructure, where $CoFe_2O_4$ (CFO, spinel) forms nanopillars embedded in the $BiFeO_3$ (BFO, perovskite) matrix,[9,10] as the

ABSTRACT In this study, advanced control of crystallographic orientations and magnetic properties of self-assembled nanostructures *via* rational selections of substrates is demonstrated. We show that in the perovskite–spinel $BiFeO_3$–$CoFe_2O_4$ model system the crystal orientation of self-assembled $CoFe_2O_4$ nanopillars can be tuned among (001), (011), and (111), while that of the $BiFeO_3$ matrix is fixed in (001). Moreover, the resultant $CoFe_2O_4$ nanopillars appear in various shapes: pyramid, roof, and triangular platform, respectively. The tunable nanostructures through this approach enable the control of material functionality such as the magnetic anisotropy of $CoFe_2O_4$. This study opens a new pathway for the engineering of self-assembled heteroepitaxial nanostructures.

model system in order to benefit from its high interface-to-volume ratio, an important parameter in coupling two materials *via* interface engineering.[11,12] In this article, we describe a novel approach to control the relative orientations of CFO and BFO by strain engineering of BFO thin films using substrates with different lattice parameters. We have succeeded in changing the orientation of CFO nanopillars while keeping that of BFO fixed. We also found that the tunability of CFO orientations leads to a shape control of these nanopillars, in which pyramid, roof, and triangular platform particles are observed. We finally demonstrate how relevant physics varies with different relative crystal orientations by showing the dependence of magnetic anisotropy of CFO nanopillars on their shape and hence their crystal orientation relative to that of BFO matrices. Our findings demonstrate a high-degree control over oxide interfaces and therefore open a new pathway to engineer and design the functionality of heteroepitaxial oxide nanostructures.

Previous studies have shown that strain states of CFO or $NiFe_2O_4$ nanopillars grown from BFO matrix are not affected much by substrates or thickness of BFO thin films,[13,14] suggesting that strain relaxation in BFO is likely a factor affecting the formation of CFO nanopillars. This hints that control of the crystallographic orientation of CFO nanopillars can be achieved by controlling the strain state of the BFO matrix. To implement this concept, we have employed strain engineering using substrates with different lattice parameters, i.e., $(001)_c$-oriented $SrTiO_3$ (STO) (a_c = 3.90 Å), $(110)_o$-oriented $DyScO_3$ (DSO) (a_{pc} = 3.94 Å), and $(110)_o$-orientated $NdGaO_3$ (NGO) (a_{pc} = 3.85 Å) (c, cubic; pc, pseudo-cubic; o, orthorhombic). These substrates were used to grow BFO−CFO self-assembled nanostructures by pulsed laser deposition (PLD) assisted with high-pressure reflective high-energy electron diffraction (RHEED). A composite target with 65% BFO and 35% CFO (molar ratio) was used, and samples were grown at 700 °C in O_2 (200 mTorr).

RESULTS AND DISCUSSION

In order to study the dynamics of phase transformation in the CFO−BFO system, we recorded the RHEED patterns, which give us in situ information about the surface structure of the sample throughout the PLD process. The structure and morphology of the film is expected to change significantly during the phase separation process. Figure 1 demonstrates such an evolution in a sample grown on $STO(001)_c$ substrate. Figure 1a,b show the predicted RHEED patterns of $BFO(001)_{pc}$ and $CFO(001)_c$, and Figure 1c−h show the experimentally recorded RHEED patterns as a function of the number of laser pulses hitting the target. Before PLD starts (Figure 1c), RHEED shows several streaks, indicating the flatness of the STO substrate. At an early stage of the PLD process (50 pulses, Figure 1d) streaks remain clear, showing a smooth thin film deposited on the substrate without the formation of any columnar structure. By increasing the number of laser pulses, the film surface becomes rough and a diffused pattern is observed (100 pulses, Figure 1e). When the pulse
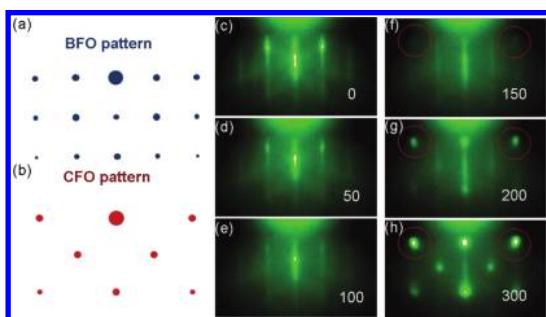

Figure 1. Calculated RHEED pattern for (a) BFO(001) and (b) CFO (001). RHEED patterns recorded as a function of number of pulses during the growth: (c) 0 pulses, (d) 50 pulses, (e) 100 pulses, (f) 150 pulses, (g) 200 pulses, (h) 300 pulses.

number hits 150, a spotted feature evolves in addition to the streaks (Figure 1f) and grows stronger when deposition is further continued (Figure 1g). The final pattern of these spots can be identified after the number of laser pulse exceeds 300 (Figure 1h). Comparing to Figure 1a and b, we found that the final RHEED pattern is the superposition of the predicted CFO pattern (spots) and a thin-film pattern (weak streaks), which results from the surface diffraction of the epitaxial BFO matrix and resembles the initial substrate pattern. The visibility of only the CFO spot pattern but the absence of the BFO pattern indicates an extrusive geometry of the CFO pillars, which is in agreement with early reported results.[8,9] Therefore, the evolution of the RHEED pattern clearly demonstrates the phase separation process of CFO nanopillars. We also found that the number of laser pulses needed to trigger the phase transformation does not depend on the growth rate or temperature, implying that the formation of CFO pillars is a nucleation-controlled process, together with ex situ analysis of the nanopillar size using atomic force microscopy (AFM).

The RHEED experiments were repeated on samples grown on $DSO(110)_o$, and $NGO(110)_o$ single-crystal substrates. We found the phase separation in these samples occurs at similar growth condition to that observed in the sample prepared on $STO(001)_c$, in all of which experiments the spotty patterns resulting from CFO are observed. The RHEED patterns of CFO−BFO heterostructures after growth on various substrates are summarized in Figure 2. Interestingly, different diffraction patterns are found in CFO nanopillars grown on different substrates: the CFO nanopillars on STO are 001 oriented (Figure 2a); the CFO nanopillars on DSO are 110 oriented (Figure 2b); the CFO nanopillars on NGO show a combination of six 111-diffraction patterns (Figure 2c). The structural information obtained from RHEED experiments is further confirmed by the studies of X-ray diffraction (XRD) on the same set of samples.

Figure 3a shows the out-of-plane XRD θ−2θ scans of samples grown on $STO(001)_c$, $DSO(110)_o$, and $NGO(110)_o$. Diffraction from BFO in all of these tested samples shows only $(00 L)_{pc}$ peaks, indicating the BFO matrix has a c-axis orientation along the surface normal of the sample regardless of what substrate is used. The lattice parameters of BFO, calculated according to the XRD angles, are 3.98, 4.04, and 4.17 Å in the films grown on DSO, STO, and NGO, respectively, indicating that BFO thin films on different substrates are subjected to different epitaxial strains due to the substrate−film lattice mismatch. However, the XRD peaks of CFO show out-of-plane orientations of $(001)_c$, $(011)_c$, and $(111)_c$ in samples grown on STO (in blue), DSO (in purple), and NGO (in green), respectively, consistent with the results obtained from RHEED experiments. The d-spacings derived from the XRD
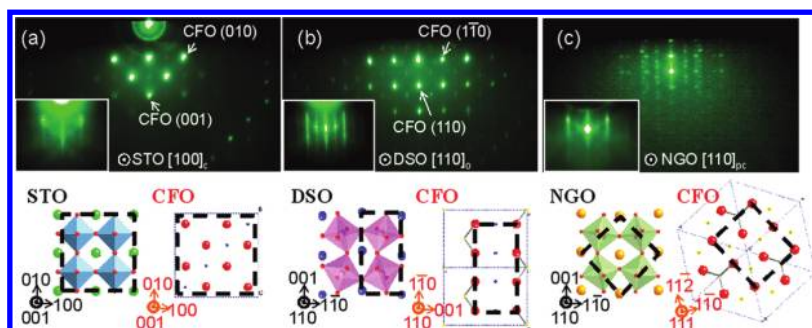
Figure 2. RHEED patterns and schematics of CoFe$_2$O$_4$–BiFeO$_3$ films grown on (a) SrTiO$_3$, (b) DyScO$_3$, and (c) NdGaO$_3$ (001)$_c$-orientated substrates. The insets show the pattern of the corresponding substrate before film growth.
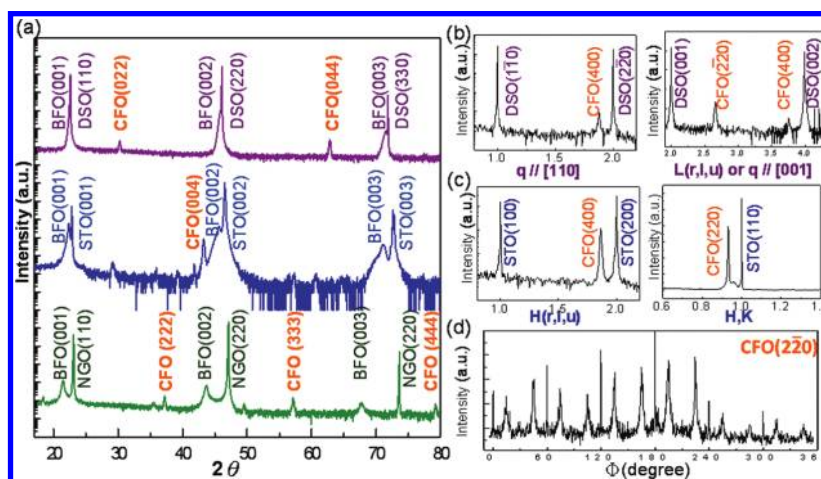

Figure 3. (a) Out-of-plane X-ray diffraction of CoFe$_2$O$_4$–BiFeO$_3$ on different substrates. (b, c) In-plane XRD of films grown on the DSO and STO substrates. (d) Phi scan of CFO on NGO substrates.

curves are 2.09 Å for CFO (004)$_c$ on STO, 2.95 Å for CFO (220)$_c$ on DSO, and 2.41 Å for CFO (222)$_c$ on NGO, all of which are very close to bulk CFO.

Detailed crystal structures of the CFO nanopillars as well as their epitaxial relationship with the substrates were further studied by in-plane grazing angle X-ray diffraction (GIXRD), performed in beamline BL17A at the National Synchrotron Radiation Research Center.

The in-plane XRD of the film on DSO shows CFO-(004)$_c$ and -(2$\bar{2}$0)$_c$ peaks when performing the scanning along DSO(1$\bar{1}$0)$_o$ direction, and 90° azimuthal rotation of the sample results in a CFO(004)$_c$ peak along the DSO(001)$_o$. This implies a two-domain structure existing in the CFO on DSO substrate, and the epitaxial relations between CFO and DSO are obtained as CFO(110)$_c$[001]$_c$||DSO(110)$_o$[001]$_o$ and CFO(110)$_c$-[1−10]$_c$||DSO(110)$_o$[001]$_o$. Further analysis shows that the intensity of the CFO(004)$_c$ peak along DSO(1$\bar{1}$0)$_o$ and the CFO(2$\bar{2}$0)$_c$ peak along DSO(001)$_o$ are stronger, and hence this is considered as the dominant domain. Since a small difference of lattice constants occurs in DSO(002)$_o$ and -(1$\bar{1}$0)$_o$, CFO(1$\bar{1}$0)$_c$ would prefer to align with DSO(002)$_c$, which have smaller lattice mismatch (Figure 3b). In the case of STO (Figure 3c), in-plane XRD scanning along STO(100)$_c$ and -(110)$_c$ shows the
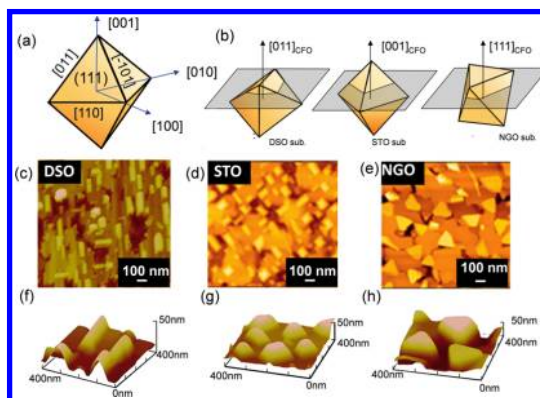

Figure 4. (a) Schematic of the lowest energy surfaces of the CFO crystal (b) Schematics of morphology of the CFO nanostructure on top of different substrates. AFM topography of BiFeO$_3$–CoFe$_2$O$_4$ films. (c–e) 2D (3 μm × 3 μm) and 3D (500 nm × 500 nm) images of the films grown on the DSO, STO, and NGO substrates.

epitaxial relation is CFO(001)$_c$[100]$_c$||STO(001)$_c$[100]$_c$, and the BFO is almost fully strained by STO, which agrees with other literature.[8,9] Only the CFO(2$\bar{2}$0)$_c$ peaks along the NGO(001)$_o$ are observed (no peak arises along the NGO(1$\bar{1}$0)$_o$) based on the in-plane XRD of CFO nanopillars on NGO (not shown). The
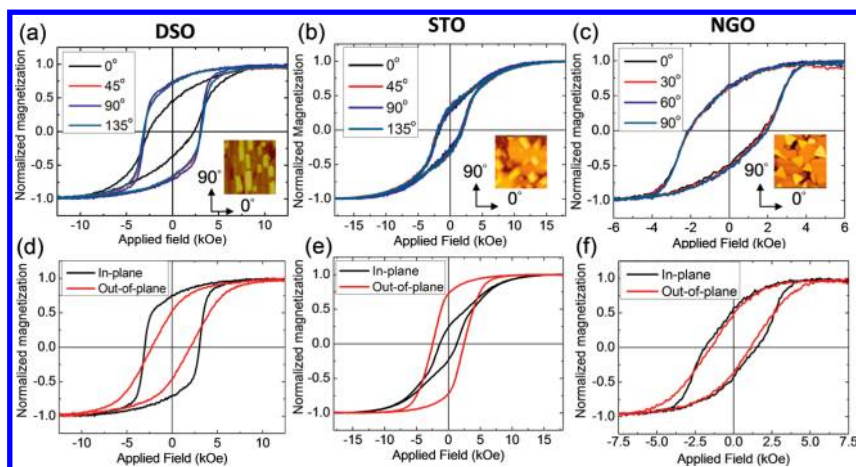
Figure 5. Magnetic hysteresis loops of BFO−CFO composite films. (a−c) Loops with different in-plane directions. (d−f) Loops with certain in-plane and out-of-plane directions of film grown on DSO, STO, and NGO substrates.

azimuthal scan (φ scan) (Figure 3d) of the CFO($2\bar{2}0$)$_c$ peak shows 18 branches from 0° to 360°, which implies six domains (3-fold symmetry) coexist in the nanopillars on NGO. Detailed analysis of the result of the φ scan shows six sharp peaks appear every 60° starting from $\varphi = 0°$ and 12 broader peaks appear every 30° starting from $\varphi = 15°$. Usually, the six narrower ones can be easily identified from the $\{2\bar{2}0\}_c$ of the 0° and 60° domains, and both domains can be found where they must have one side of the three edges parallel to the NGO(001)$_o$, which describes the epitaxial relationship of CFO(111)$\langle1\bar{1}0\rangle_c$||NGO-(110)$_o(001)_o$. However, there are still 12 broader ones presented in the φ scan, and they can be distinguished as four domains, where two domains related to 0° and 60° domains are rotated by $\varphi = 15°$, and the other two domains are rotated by $\varphi = -15°$. Therefore, the epitaxy between these four domains of CFO and NGO can be derived as CFO(111)$_c\langle11\bar{2}\rangle_c$||NGO(110)$_o$($1\bar{1}2$)$_o$.

With the understanding of the crystallographic orientations and epitaxial relationships of the CFO−BFO heterostructures on different substrates, we now discuss the morphologies of the nanopillars in these samples. It is understood that the spinel crystal prefers to form an octahedron with eight (111) surfaces, as shown in Figure 4a, because of the lowest surface energy at these planes.[15] In this case, the morphology appears to be different when the octahedron orients differently (Figure 4b): A 001-oriented octahedron emerges as a pyramid-like particle; a 011-oriented octahedron emerges as a roof-like particle; a 111-oriented octahedron emerges as a triangle-platform particle. This logic is confirmed by the AFM studies on the surface topography of the BFO−CFO heterostructures on DSO, STO, and NGO, where roof-like (~50 nm), pyramid-like (~70 nm), and triangle-platform particles (~150 nm) are observed, respectively (Figures 4c−e). The morphology control had been demonstrated by changing the substrate orientation,[8,16] but this is the first time to show this change while keeping the matrix in one single crystallographic orientation. In addition, the results obtained

from AFM are consistent with data from GIXRD. For example, the edge of the pyramid and roof is parallel to CFO(011). Thus, according to the AFM images shown in Figure 4a and b the epitaxial relations between CFO and the substrates are CFO[110]||STO[110] and CFO[$1\bar{1}$0]|| DSO[002]$_o$. In the case of CFO on NGO, six orientations are observed in the triangular CFO islands. Among them, one edge of two orientations is parallel to NGO[001]$_o$, and the other four have a 15° rotation from the NGO[001]$_o$. This conclusion is in full agreement with the GIXRD results.

Finally, we demonstrate the control of magnetic anisotropy of the CFO−BFO heterostructure through the control of shape anisotropy of CFO.[17] While magnetocrystalline anisotropy, magnetostriction anisotropy, and shape anisotropy can all contribute to magnetic anisotropy, the shape anisotropy dominates in the CFO−BFO system because the cubic symmetry of CFO results in a little anisotropy between the in-plane and out-of-plane directions and the relaxed CFO nanopillars cannot generate magnetostriction anisotropy. Figure 5 shows the magnetic properties, measured by vibrating sample magnetometer (VSM), of the samples grown on different substrates with different CFO orientations. Figure 5a−c show the hysteresis loops measured in in-plane directions, and Figure 5d−f show the hysteresis loops measured in one of the in-plane and out-of-plane directions. It is found that the magnetic easy axis of the CFO nanopillars on STO is along the STO[001]$_c$ (out-of-plane), while the magnetic easy axis of the CFO nanopillars on DSO is along the DSO[001]$_o$ (in-plane). As for CFO on NGO, no magnetic anisotropy in any direction is observed. For the STO and DSO cases, the long axis of the islands is STO[001]$_c$ and DSO[001]$_o$, respectively. This agreed very well with the magnetic easy axis we obtained from the measurements. The magnitude of anisotropy is the same as the calculated shape anisotropy with spheroid approximation.[18] The six in-plane orientations of CFO nanopillars on NGO and the size of these triangular islands similar to film thickness result in

no obvious shape anisotropy. Tunability of magnetic anisotropy has been clearly shown; therefore, it is possible to design a suitable combination of orientations for the phases in vertical nanostructures to enhance the functionality.

SUMMARY

In summary, we have taken the perovskite—spinel BFO—CFO self-assembled heteroepitaxial nanostructures as a model system to demonstrate the capability of control of relative orientations of the constituent materials in the heterostructures. We have achieved control by tuning the strain state of the BFO matrix and hence created CFO nanopillars with different crystal orientations, different shapes, and different magnetic anisotropies. The presented results experimentally prove the concept that the novel properties in oxide heterostructures can be tuned by controlling their interfacial structures.

METHODS

BFO—CFO self-assembled nanostructures used in this study are fabricated by pulsed laser deposition with a 248 nm KrF laser, assisted with high-pressure reflective high-energy electron diffraction. A composite target with 65% BFO and 35% CFO (molar ratio) was used, and samples were grown at 700 °C in O_2 (200 mTorr). No annealing process is used for all samples. High-resolution out-of-plane and grazing-angle in-plane X-ray diffraction was taken with the BL17A at the National Synchrotron Radiation Research Center (NSRRC). Topography studies were performed using a Veeco EnviroScope operating in tapping mode. Magnetic hysteresis loop was taken with a Princeton Measurement Corporation model 3900 VSM. For microstructures grown on DSO and NFO substrates, the substrate was milled from the backside before VSM measurement to remove the magnetic signal from the substrate, and data were checked with X-ray magnetic dichroism on the Co-edge taken in the BL09A at NSRRC.

REFERENCES AND NOTES

1. Takagi, H.; Hwang, H. Y. An Emergent Change of Phase for Electronics. *Science* **2010**, *327*, 1601–1602.
2. Wu, S. M.; Cybart, S. A.; Yu, P.; Rossell, M. D.; Zhang, J. X.; Ramesh, R.; Dynes, R. C. Reversible Electric Control of Exchange Bias in a Multiferroic Field-Effect Device. *Nat. Mater.* **2010**, *9*, 756–761.
3. Ohtomo, A.; Hwang, H. Y. A High-Mobility Electron Gas at the $LaAlO_3/SrTiO_3$ Heterointerface. *Nature (London, U. K.)* **2004,** *427*, 423–426.
4. Chakhalian, J.; Freeland, J. W.; Srajer, G.; Strempfer, J.; Khaliullin, G.; Cezar, J. C.; Charlton, T.; Dalgliesh, R.; Bernhard, C.; Cristiani, G.; *et al.* Magnetism at the Interface Between Ferromagnetic and Superconducting Oxides. *Nat. Phys.* **2006,** *2*, 244–248.
5. Zheng, H.; Wang, J.; Lofland, S. E.; Ma, Z.; Mohaddes-Ardabili, L.; Zhao, T; Salamanca-Riba, L.; Shinde, S. R.; Ogale, S. B.; Bai, F.; *et al*. Multiferroic $BaTiO_3$-$CoFe_2O_4$ Nanostructures. *Science (Washington, DC, U. S.)* **2004**, *303*, 661–663.
6. Lee, H. N.; Christen, H. M.; Chisholm, M. F.; Rouleau, C. M.; Lowndes, D. H. Strong Polarization Enhancement in Asymmetric Three-Component Ferroelectric Superlattices. *Nature (London, U. K.)* **2005**, *433*, 395–399.
7. Ueda, K.; Tabata, H.; Kawai, T. Ferromagnetism in $LaFeO_3$-$LaCrO_3$ Superlattices. *Science (Washington, DC, U. S.)* **1998,** *280*, 1064–1066.
8. Zheng, H.; Straub, F.; Zhan, Q.; Yang, P. L.; Hsieh, W. K.; Zavaliche, F.; Chu, Y. H.; Dahmen, U.; Ramesh, R. Self-Assembled Growth of $BiFeO_3$—$CoFe_2O_4$ Nanostructures. *Adv. Mater. (Weinheim, Ger.)* **2006**, *18*, 2747–2752.
9. Zheng, H.; Zhan, Q.; Zavaliche, F.; Sherburne, M.; Straub, F.; Cruz, M. P.; Chen, L. Q.; Dahmen, U.; Ramesh, R. Controlling Self-Assembled Perovskite-Spinel Nanostructures. *Nano Lett.* **2006**, *6*, 1401–1407.
10. Muralidharan, R.; Dix, N.; Skumryev, V.; Valera, M.; Sanchez, F.; Fontcuberta, J. Synthesis, Structure, and Magnetic Studies on Self-Assembled $BiFeO_3$—$CoFe_2O_4$ Nanocomposite Thin Films. *J. Appl. Phys.* **2008,** *103*, 07E301–07E303.
11. Nan, C. W. Magnetoelectric Effect in Composites of Piezoelectric and Piezomagnetic Phases. *Phys. Rev. B: Condens. Matter Mater. Phys.* **1994,** *50*, 6082–6088.
12. Mac-Manus-Driscoll, J. L. Self-Assembled Heteroepitaxial Oxide Nanocomposite Thin Film Structures: Designing Interface-Induced Functionality in Electronic Materials. *Adv. Funct. Mater.* **2010,** *20*, 2035–2045.
13. Dix, N.; Muralidharan, R.; Rebled, J. M.; Estrade, S.; Peiro, F.; Varela, M.; Fontcuberta, J.; Sanchez, F. Selectable Spontaneous Polarization Direction and Magnetic Anisotropy in $BiFeO_3$-$CoFe_2O_4$ Epitaxial Nanostructures. *ACS Nano* **2010**, *4*, 4955–4961.
14. Crane, S. P.; Bihler, C.; Brandt, M. S.; Goennenwein, S. T. B.; Gajek, M.; Ramesh, R. Tuning Magnetic Properties of Magnetoelectric $BiFeO_3$—$NiFe_2O_4$ Nanostructures. *J. Magn. Magn. Mater.* **2009**, *321*, L5–L9.
15. Mishra, R. K.; Thomas, G. Surface Energy of Spinel. *J. Appl. Phys.* **1977,** *48*, 4576–4580.
16. Levin, I.; Li, J. H.; Slutsker, J.; Roytburd, A. L. Design of Self-Assembled Multiferroic Nanostructures in Epitaxial Films. *Adv. Mater. (Weinheim, Ger.)* **2006**, *18*, 2044–2047.
17. Bozorth, R. M.; Tilden, E. F.; Williams, A. J. Anisotropy and Magnetostriction of Some Ferrites. *Phys. Rev.* **1955**, *99*, 1788–1798.
18. Osborn, J. A. Demagnetizing Factors of the General Ellipsoid. *Phys. Rev.* **1945,** *67*, 351–357.